Proceedings of the 2023
30th International Conference on Nuclear Engineering
ICONE30
May 21-26, 2023, Kyoto, Japan

ICONE30-1211

A TURBULENCE MODEL SENSITIVITY ANALYSIS OF THERMAL-HYDRAULIC PROPERTIES ON THE PRE-CONCEPTUAL NIST NEUTRON SOURCE DESIGN

Joy Shen
NIST Center for
Neutron Research
Gaithersburg, MD

Abdullah G. Weiss
NIST Center for
Neutron Research
Gaithersburg, MD

Anil Gurgen
NIST Center for
Neutron Research
Gaithersburg, MD

Idan R. Baroukh
Nuclear Research
Center in Negev
Negev, Israel

ABSTRACT

The current reactor at the NIST, the National Bureau of Standards Reactor (NBSR) was first critical in 1967, serving as a premiere user-facility to the international neutron scattering research community. The NBSR's age has contributed to difficulties like longer outage times and increased maintenance costs, prompting an investigation of a new design to replace it. The proposed replacement, the NIST Neutron Source (NNS), is the focus of this paper, which investigates the thermal-hydraulic behavior of the NNS' compact core preliminary design using computational fluid dynamics (CFD) analysis. While developing the CFD model, any flow irregularities may significantly affect thermal-hydraulic characteristics such as the core's pressure or velocity profiles. Therefore, a turbulence model must be carefully selected to balance computational costs and model uncertainties. This paper details a sensitivity analysis that compares various Reynolds Averaged Navier stokes (RANS) turbulence models in ANSYS Fluent® including k-ε, k-ω, k-ω SST, realizable k-ε and Spallart-Allmaras. The resulting velocity and pressure profiles of the coolant flowing from the inlet plenum of the core are compared for fit. Discussions of the mesh, assumptions, and boundary conditions are also provided in the text, demonstrating the limitations and methodologies of the study.

Keywords: NNS; CFD; Turbulence; Hydraulics; Sensitivity

NOMENCLATURE

C_P	Coefficient of pressure
D	Hydraulic diameter
k	Turbulent kinetic energy
P	Pressure
U	Spanwise (horizontal) velocity
V	Streamwise (vertical) velocity
V_∞	Inlet/bulk velocity
X	Spanwise (horizontal) location
Y	Streamwise (vertical) location
ρ	Fluid density
ν	Fluid kinematic viscosity
ν_t	Turbulent (eddy) viscosity
ϵ	Dissipation rate of k
ω	Specific dissipation rate of k

1. INTRODUCTION

The reactor at NIST's Center for Neutron Research (NCNR), or the National Bureau of Standards Reactor (NBSR) has been operational for over 50 years. In this time, the reactor has provided cold and thermal neutron scattering for the international neutron physics community. However, its age may have effects on plant maintenance, and efficiency as seen in an increase in outage time and maintenance costs. Preliminary efforts have been launched to propose a new reactor design, namely the NIST neutron source (NNS) [1-2], which requires an analysis on the conceptual core's thermal-hydraulics behavior. Several previous [3] and ongoing [4] works have investigated the preliminary thermal-hydraulics behavior. A notable previous analysis [5] performed preliminary investigations on the flow behavior in the core using simplified computational fluid dynamics (CFD) models in ANSYS® FLUENT commercial code [6], where it was found that additional efforts are needed to characterize the inlet region preceding the fuel assemblies.

This work focuses on simulating the inlet region to the core and describing the resulting velocity and pressure behaviors throughout the geometry. Multiple Reynolds-Averaged Navier-Stokes (RANS) models are adopted in this work, namely k-ϵ, k-ω, k-ω SST, realizable k-ϵ, and Spallart-Allmaras. The results from each model will be compared using spanwise traces to better communicate the variations between each of the models and where discrepancies arise.

2. METHODOLOGY

The NNS preconceptual design has 9 fuel assemblies in a 3x3 arrangement, including 4 reactivity safety blades and 2 reactivity control blades between the fuel assemblies. There are 21 curved fuel plates per fuel assembly, resulting in a total of 64 flow channels in each row of the core. The core is cooled with an upwards forced flow of light-water. Figure 1 shows a 3-dimensional representation of the core, where three distinct regions are identified: 1. the inlet region, 2. the active height, and 3. the outlet region. The active height consists of an array of separated rectangular channels, thus it is possible to simulate all the channels using a single model with varying inlet and boundary conditions based on the expected behavior from the inlet region and the power peaking of the fuel plates that act as boundary conditions to the coolant channels. The outlet is a mixing plenum that is of less relevance to fuel cooling and safety.

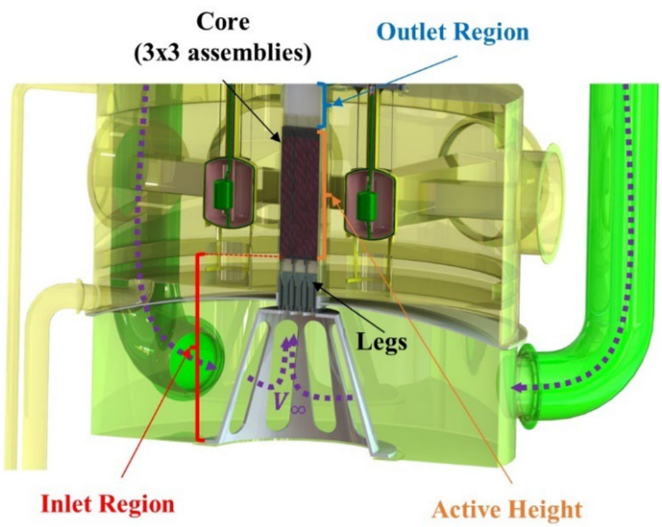

FIGURE 1: CORE LAYOUT AND FLOW GEOMETRY.

The inlet region is the most critical portion of the geometry, as it dictates the inlet behavior to each channel providing cooling to the fuel plates. Although the geometry is not particularly complex, the presence of the legs from the lower grid plate forces a flow separation through the legs, and a downstream intermediate mixing region prior to separating again to each fuel assembly and its coolant channels. This anticipated separation-mixing-separation behavior provides concerns of adverse pressure gradients and notable velocity gradients that could affect the cooling efficiency of the fuel plates in the core. This could lead to, for example, insufficient cooling in some fuel assemblies, and over-cooling in other assemblies. To further investigate these problems, this work focuses on simulating a steady-state model of the inlet region only.

2.1 Mesh Setup

This work adopts a 2-dimensional representation of the inlet region geometry, per Figure 2. A simple mesh convergence study was performed by increasing the number of elements until a solution was converged upon. A total of 48,140 hexahedral elements were converged upon, with 97,920 nodes as shown in Figure 2. The mesh exhibits a maximum skewness of approximately 0.108, and y^+ is between 0.05 and 0.25 cm at the elements near the wall. The higher y^+ is used in the lower portions of the geometry that is uninterrupted leading to the legs where the flows separate. At the legs, the y^+ varies between 0.05 cm to 0.25 cm. This range persists as the flow progresses towards the active height (top of the simulated geometry). Note that this desirable y^+ is achieved by separating the geometry into blocks, wherein the number of elements is increased iteratively until the streamwise velocity (V) solution converges to within 10^{-4} m/s (according to results in the standard k-ϵ model). This mesh was generated and refined in OpenFOAM [7], which is utilized as part of an in-depth verification & validation effort for the NNS CFD modeling activities.

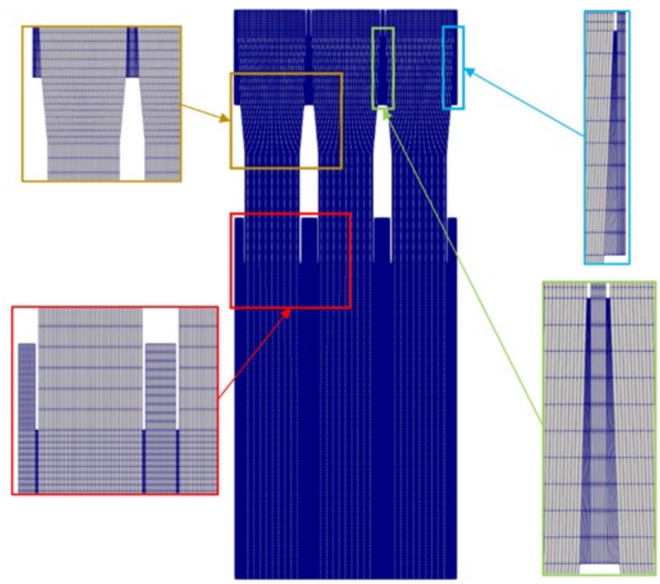

FIGURE 2: THE MESH UTILIZED IN THIS WORK FOR THE INLET REGION.

With this mesh configuration, the y^+ towards the top of the geometry should be capable of capturing some of the physics in the viscous sublayer of the turbulent boundary layers, but this study is not expected to provide such high fidelity understanding of the flow behavior. It is deemed more appropriate to have a comparison to higher fidelity turbulence models, such as a Large Eddy Simulation (LES) model before properly assessing the turbulent boundary layer behavior near the walls. It is also not entirely relevant to the design of the reactor to assess the turbulent boundary layer in the inlet region, so there is a possibility that it may not be revisited in future works. With the provided mesh, multiple turbulence models are utilized to simulate the flow.

2.2 Model Setup

RANS models utilize the mean velocity along the i-th spatial dimension (U_i) and pressure (P) equations shown in equations (1) and (2), which correspond to the conservation of momentum and mass, respectively. These equations show averaged forms of U_i and P ($\langle U_i \rangle$ and $\langle P \rangle$, respectively alongside a viscosity (kinematic viscosity ν in this case due to the absence of density ρ from the equations). It should be noted that an additional unknown in the form of Reynolds stresses $\langle u_i u_j \rangle$ prevents one from realistically solving the equations, and as such, another equation, or closure model for $\langle u_i u_j \rangle$ is needed to solve, which comes in the form of the Boussinesq approximation shown in equation (3) [8-9].

$$\frac{\partial \langle U_i \rangle}{\partial t} + \langle U_j \rangle \frac{\partial \langle U_i \rangle}{\partial x_j} = -\frac{\partial \langle P \rangle}{\partial x_i} - \frac{\partial \langle u_i u_j \rangle}{\partial x_j} + \nu \frac{\partial^2 \langle U_i \rangle}{\partial x_j \partial x_i} \tag{1}$$

$$\frac{\partial^2 \langle P \rangle}{\partial x_j \partial x_j} = -2 \frac{\partial \langle U_i \rangle}{\partial x_j} \frac{\partial \langle U_j \rangle}{\partial x_i} - \frac{\partial^2 \langle u_i u_j \rangle}{\partial x_j \partial x_j} \tag{2}$$

$$\langle u_i u_j \rangle = \frac{2}{3} k\, \delta_{ij} - \nu_t \left(\frac{\partial \langle U_i \rangle}{\partial x_j} + \frac{\partial \langle U_j \rangle}{\partial x_i} \right) \tag{3}$$

The Boussinesq approximation yields two new unknowns, the turbulent kinetic energy (k) and the turbulent viscosity (ν_t), which will require additional transport equations. Each turbulence model uses different closure equations, the most common of which are 2-equation models like the k-ϵ (standard) model [10] shown in equations (4) and(5). Note that in k-ω, it is also possible to represent ν_t as a function of the model coefficient C_μ per equation (6), where ϵ is the dissipation rate of k. Note the presence of other model coefficients, all of which have the constant values shown in Table 1.

$$\frac{\partial k}{\partial t} + \langle U_j \rangle \frac{\partial k}{\partial x_j} = -\langle u_i u_j \rangle \frac{\partial \langle U_i \rangle}{\partial x_j} - \epsilon + \frac{\partial}{\partial x_j} \left[\left(\nu + \frac{\nu_t}{\sigma_k} \right) \frac{\partial k}{\partial x_j} \right] \tag{4}$$

$$\frac{\partial \epsilon}{\partial t} + \langle U_j \rangle \frac{\partial \epsilon}{\partial x_j} = -C_{\epsilon 1} \frac{\epsilon}{k} \langle u_i u_j \rangle \frac{\partial \langle U_i \rangle}{\partial x_j} - C_{\epsilon 2} \frac{\epsilon^2}{k} + \frac{\partial}{\partial x_j} \left[\left(\nu + \frac{\nu_t}{\sigma_\epsilon} \right) \frac{\partial \epsilon}{\partial x_j} \right] \tag{5}$$

$$\nu_t = C_\mu \frac{k^2}{\epsilon} \tag{6}$$

Another popular two equation model is the k-ω model [11], which is shown in equations (7) and(8). In this model, the ν_t is represented as shown in equation (9) as a function of the specific dissipation rate ω. Note the similarities between k-ϵ and k-ω, where β^* is essentially a substitute for C_μ in the k-ω model. The model constants are listed in Table 1.

$$\frac{\partial k}{\partial t} + \langle U_j \rangle \frac{\partial k}{\partial x_j} = -\langle u_i u_j \rangle \frac{\partial \langle U_i \rangle}{\partial x_j} - \beta^* k \omega + \frac{\partial}{\partial x_j} \left[(\nu + \nu_t \sigma^*) \frac{\partial k}{\partial x_j} \right] \tag{7}$$

$$\frac{\partial \epsilon}{\partial t} + \langle U_j \rangle \frac{\partial \epsilon}{\partial x_j} = -\alpha \frac{\omega}{k} \langle u_i u_j \rangle \frac{\partial \langle U_i \rangle}{\partial x_j} - \beta \omega^2 + \frac{\partial}{\partial x_j} \left[\left(\nu + \frac{\nu_t}{\sigma} \right) \frac{\partial \omega}{\partial x_j} \right] \tag{8}$$

$$\nu_t = \frac{k}{\omega} = \beta^* \frac{k^2}{\epsilon} \tag{9}$$

Another relevant turbulence model that is well utilized in various works is the Spalart-Allmaras (SA) model, which is a one equation ν_t transport model of the form shown in equation (10). Note that there this model heavily depends on multiple constants, most of which are listed in Table 1 for the reader's convenience. For the sake of brevity, the reader is directed to Spalart and Allmaras's original work [12] for additional information on the model, and it should be noted that the original coefficients used by Spallart and Allmaras are used in this work as well. The Dacles-Mariani modification [13] was not used in this work.

$$\frac{\partial \tilde{\nu}}{\partial t} + \langle U_j \rangle \frac{\partial \tilde{\nu}}{\partial x_j} = -c_{b1} \tilde{S} \tilde{\nu} - c_{w1} f_w \left(\frac{\tilde{\nu}}{d} \right)^2 + \frac{1}{\sigma} \frac{\partial}{\partial x_k} \left[(\nu + \tilde{\nu}) \frac{\partial \tilde{\nu}}{\partial x_k} \right] + \frac{c_{b2}}{\sigma} \frac{\partial \tilde{\nu}}{\partial x_k} \frac{\partial \tilde{\nu}}{\partial x_k} \tag{10}$$

Two additional models are utilized in the form of k-ω Shear Stress Transport (SST) [14] model and the Realizable k-ϵ model [15], which will be referred to as SST and RKE hereafter for briefness, respectively. The SST is a variant of the standard k-ω model that substitutes standard k-ω with the standard k-ϵ model in the freestream. This is done via a simple substitution between ϵ and ω near and away from the walls of the domain, which yields an additional cross-diffusion term between k and ω that uses a blending function to provide a smooth transition between standard k-ω near the wall to standard k-ϵ in the freestream. The ν_t is defined differently in the SST model per equation (11). SST model includes the influence of the shear stress component like the half-equation model of Johnson and King [16], which improves its performance with flows possessing strong adverse pressure gradients.

$$\nu_t = \frac{\alpha_1 k}{\max(\alpha_1 \omega,\ S F_2)}, \quad \begin{cases} \alpha_1 = \frac{5}{9} \\ F_2 = \tanh\left(\left[\max\left(\frac{2\sqrt{k}}{\beta^* \omega y}, \frac{500\nu}{y^2 \omega} \right) \right]^2 \right) \\ S = \frac{\omega}{k} \langle u_i u_j \rangle \frac{\partial \langle U_i \rangle}{\partial x_j} \end{cases} \tag{11}$$

The RKE model [15] is a variant of standard k-ϵ that reformulates the ϵ transport equation and includes a dynamic treatment for C_μ to satisfy realizability of the Reynolds stresses. These alterations in k-ϵ enable greater generalizability and make the model applicable to significantly more complex flows. The fact that C_μ is a non-constant quantity enables greater sensitivity of the model to flow topology and improves the prediction of mean flow quantities [17]. Per equation (12), the C_μ in the RKE model is a function of the shear velocity U^* and a couple of unique model constants, namely A_0 and A_s. Note that A_s depends on the shear stress ratio W, which is detailed in literature [18].

$$C_\mu = \frac{1}{A_0 + A_s \frac{k U^*}{\epsilon}}, \quad \begin{cases} A_0 = 4.04 \\ A_s = \sqrt{6} \cos\left(\frac{1}{3} \cos^{-1}\left(\sqrt{6}\, W \right) \right) \end{cases} \tag{12}$$

TABLE 1: THE MODEL COEFFICIENTS FOR EACH RANS MODEL USED IN THIS WORK.

k-ϵ	C_μ	$C_{\epsilon 1}$	$C_{\epsilon 2}$	σ_k	σ_ϵ			
	0.09	1.44	1.92	1.0	1.3			
k-ω	β^*	α	β	σ^*	σ			
	0.09	0.5	0.075	0.5	0.5			
SA	C_{b1}	C_{b2}	C_{v1}	σ	C_{w1}	C_{w2}	C_{w3}	κ
	0.14	0.62	7.1	2/3	3.24	0.3	2.0	0.41

With the turbulence models defined, it is now relevant to consider the user inputs and boundary conditions applied in this work, which are identical for all of the models. The boundary conditions are listed in Table 2. It is important to point out that the density of the fluid is $\rho = 990.8$ kg/m^3, the kinematic viscosity is $\nu = 6.19\times10^{-7}$ m^2/s, the hydraulic diameter is $D = 24.65$ cm, and the inlet velocity is $V_\infty = 12.78$ m/s. A turbulence intensity (T_i) of 10 % is assumed, which enables the computation of bulk values of k, ϵ and ω that can also be used at the inlet. The subscript ∞ is used to denote a bulk or inlet value of a variable. The bulk turbulent kinetic energy (k_∞) is computed per equation (13), which then allows for the computation of ω_∞ and ϵ_∞ per equation (6) or equation (9). The bulk turbulent viscosity ($\nu_{t,\infty}$) is assumed to be 15 times the ν ($\nu_{t,\infty} \sim 15\nu$).

$$k_\infty = \frac{3}{2}(T_i \cdot V_\infty) \tag{13}$$

TABLE 2: THE BOUNDARY CONDITIONS USED.

Variable	Inlet	Outlet	Walls
U	$U = 0$	$\frac{\partial U}{\partial x_i} = 0$	No Slip
V	V_∞	$\frac{\partial V}{\partial x_i} = 0$	No Slip
P	$\frac{\partial P}{\partial x_i} = 0$	$P = 0$	$\frac{\partial P}{\partial x_i} = 0$
k	k_∞	$\frac{\partial k}{\partial x_i} = 0$	$\frac{\partial k}{\partial x_i} = 0$
$\epsilon,\ \omega$	$\epsilon_\infty,\ \omega_\infty$	$\frac{\partial\{\epsilon,\omega\}}{\partial x_i} = 0$	Wall function
ν_t	$\nu_{t,\infty}$	$\nu_{t,\infty}$	Wall function

Wall functions are used for ω and ϵ to calculate their values at the wall based on an average of their value in the nearby cells. The ν_t also utilizes a wall function that dictates its value at the wall based on the k and y^+, where the ν_t is set to zero when the cell reaches intersection between the viscous and the logarithmic sublayers in the boundary layer. Note that the popular convention of U being the horizontal velocity and V being the vertical velocity is adopted in this work. The results are non-dimensional in this work, where either velocity component is normalized by dividing with V_∞, and P is normalized with respect to the dynamic pressure at the inlet, yielding the coefficient of pressure (C_P) per equation (14).

$$C_P = \frac{2P}{\rho V_\infty^2} \tag{14}$$

3. RESULTS AND DISCUSSION

The profiles shown in Figure 3 illustrate the evolution of the non-dimensionalized streamwise velocity (V/V_∞) in each of the investigated turbulence models. The velocities vary in the ranges shown in Table 3 for each of the given models. On average, the deviation is in the range of -0.29 ($\pm$22%)$\leq V/V_\infty \leq$1.7 ($\pm$2.2%). The displayed uncertainties represent the standard deviation (σ) in the minimum and maximum values of the field divided by their average value (μ), respectively. Note the significantly larger deviation in V/V_∞ is in the counterflow (negative velocities), which indicates that the models vary in their interpretation of regions with prominent eddies. This is an expected limitation for any RANS model and is reported in various works [19]. The extent to which this discrepancy arises is concerning however, where regions with eddies have upwards of 22% uncertainty in the streamwise velocity. This has some serious implications regarding flow separation and mixing behaviors in the geometry, where the recirculation zones and regions of adverse pressure gradients may not be determined purely with RANS models.

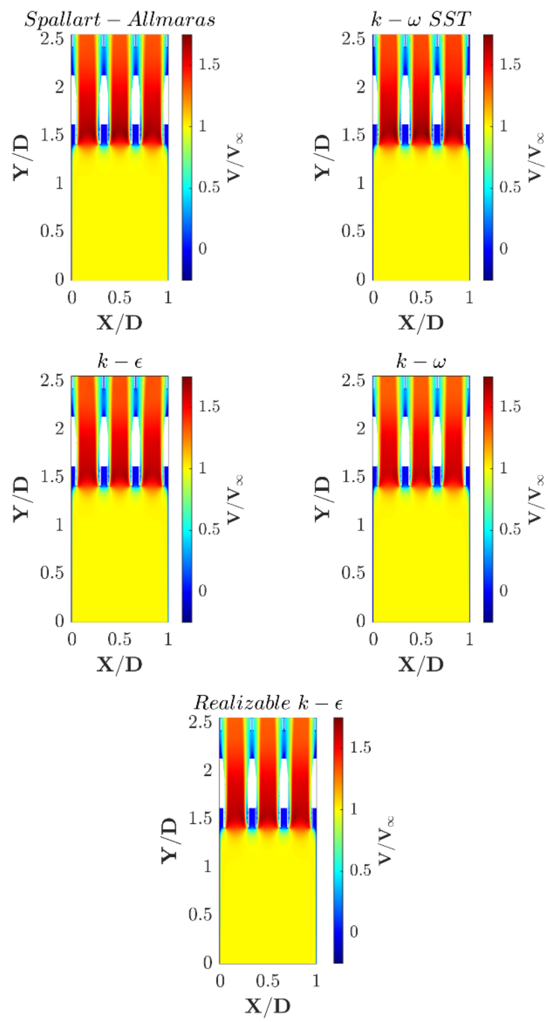

FIGURE 3: THE V/V_∞ FIELD FOR EACH INVESTIGATED MODEL.

The non-dimensionalized spanwise velocity (U/V_∞) profiles for each model are shown in Figure 4. The regions with the largest recirculation zones, and the largest eddies, are at the bottom edge of the legs where the flow separates into each leg. This is important to note as it allows us to understand how and where the mesh should be further refined. However, the largest variations between the turbulence models are found in the region between the outlets of the legs and the fuel assemblies' inlet, which is found in Y/D between 2.15 and 2.4 (which will be referred to hereafter as the intermediate mixing plenum). The mixing plenum is also the region where the largest V/V_{∞} deviations between the models are observed. The deviations sometimes exceed by 100% in specific locations in the intermediate mixing plenum, specifically in the regions between each pair of fuel assemblies (which is in the two X/D ranges from 0.3 to 0.36 and 0.64 and 0.7). However, on average the deviation between the models is within a range from -0.93 to 0.934. Further details are given in Table 3.

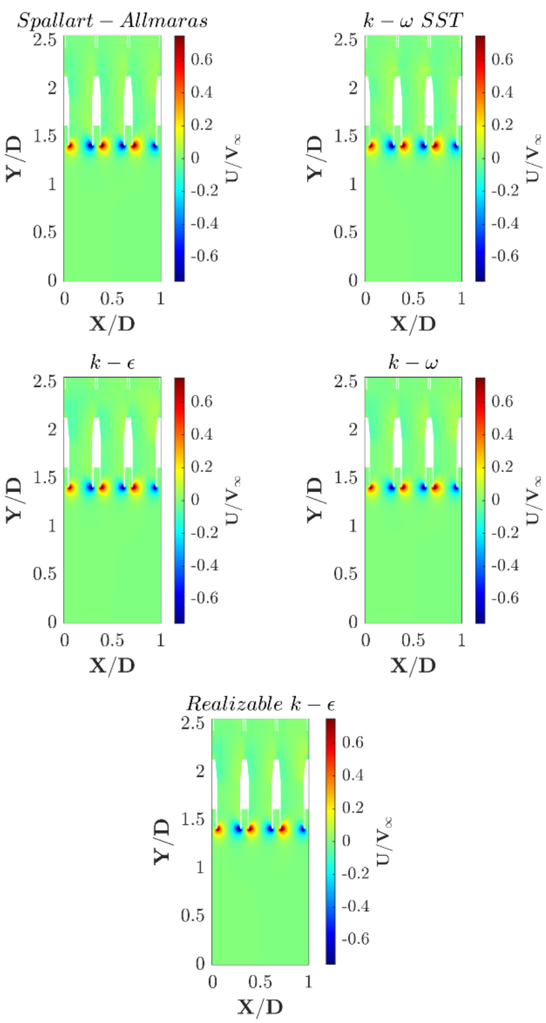

FIGURE 4: THE U/V_{∞} FIELD FOR EACH INVESTIGATED MODEL.

The C_P profiles for each of the investigated models are shown in Figure 5, where the largest pressure gradients can be seen in the same regions where the U/V_{∞} and V/V_{∞} profiles experienced the largest model-to-model deviation. This of course includes the aforementioned X/D locations in the intermediate mixing plenum, but they also demonstrate adverse gradients near the walls of the legs. These gradients are likely brought-by the separation that occurs upstream of the legs, which in-fact starts at X/D approximately 0.4, roughly $1D$ upstream of the legs. This is relevant because it allows one to understand how much of the domain upstream of the legs is vital to accurately assessing the flow behavior in the rest of the flow. An interesting observation is the notably lighter color of C_P in the k-ω profile, which is notable because the k-ω model seems to have the greatest deviation with all other models. Curiously enough, the k-ω model's C_P prediction disagrees the most with the SST variant's prediction, where the deviation can be ~5% in the bulk flow throughout the geometry. On the other hand, the k-ω standard model's bulk C_P prediction is closest to realizable k-ϵ, where the C_P predictions of both models are within ~1% of one-another.

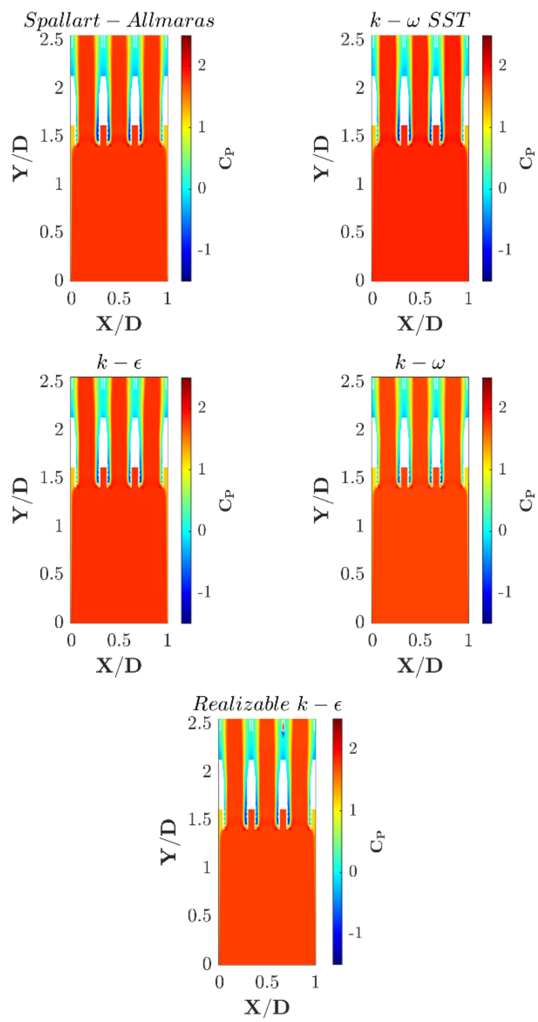

FIGURE 5: THE C_P FIELD FOR EACH INVESTIGATED MODEL.

On average, the deviation between the models C_p between -1.75 and 2.22 per Table 3. A summary of the results and the variations (based on the maximum and minimum values in the profiles) are shown in Table 3. Note that the values in Table 3 only communicate a portion of the story, where additional variations can be found once considering the statistics of the entire geometry, which should be further investigated in future works.

TABLE 3: THE VARIATION OF RELEVANT VELOCIMETRIC VARIABLES IN EACH INVESTIGATED MODELS.

Model	V/V_∞		U/V_∞		C_P	
	min	max	min	max	min	max
SA	-0.376	1.738	-0.935	0.932	-1.774	2.190
k-ω SST	-0.343	1.744	-0.936	0.930	-1.721	2.244
k-ϵ	-0.245	1.692	-0.926	0.931	-1.720	2.133
k-ω	-0.248	1.651	-0.944	0.944	-1.793	2.110
Rk-ϵ	-0.240	1.695	-0.937	0.931	-1.759	2.398
Average (μ)	-0.290	1.704	-0.936	0.934	-1.753	2.215
σ/μ (%)	-22.14%	2.24%	0.69%	0.60%	-1.85%	5.17%

To enable a more quantitative analysis, spanwise velocity profiles for U/V_∞, V/V_∞, and C_p at multiple streamwise locations are given in Figures 4 through Figure6, respectively. The streamwise evolution of these profiles are extracted at six Y/D trace locations of interest. These traces describe regions regarding coolant separation and mixing as described in Table 4 and visualized in the V/V_∞ contour in Figure 6.

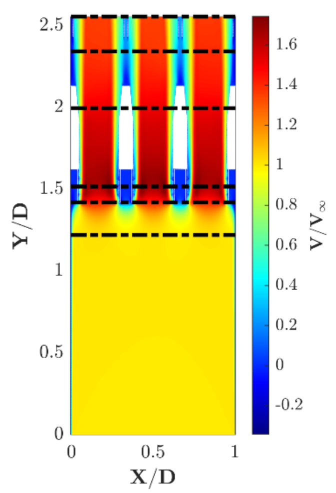

FIGURE 6: THE TRACE LOCATIONS CAPTURED IN THIS WORK. NOTE THAT THIS V/V_∞ FIELD IS FROM THE k-ω SST MODEL.

TABLE 4: TRACE LOCATIONS AND DESCRIPTIONS.

Trace	Y/D	Description
1	1.2	Directly upstream of separation from legs
2	1.4	Start of separation
3	1.5	Directly downstream of separation
4	2	Directly upstream of mixing
5	2.3	~0.15 Y/D into the mixing
6	2.6	Directly upstream of active height

Figure 7 shows the V/V_∞ profiles at each of the traces listed in Table 4. The profiles visualize the very minimal disagreement between the models due to the wide range of velocities, but the variations observed in Table 3 persist here as well. Although, it is noted that the variations cannot be qualitatively discerned. Although this shows minimal disagreement, this only tells a portion of the story, as the U/V_∞ and C_P profiles would show more differences. Specifically in the intermediate mixing plenum. Regardless of how dull the profiles in Figure 7 may seem (due to their strong agreement), it is important to note this practical lack of disagreement here. Hence, it may not be necessary to investigate any other velocity components or flow phenomena other than the streamwise velocity profiles of V/V_∞. Consider, for example, a model of the NNS using a system code with limited dimensionality. It is highly likely that a system code would be used for accident analyses anyways, and for that code, it is mainly relevant to know the inlet flowrate into each of the coolant channels, which can be found by simply extracting the profiles shown in Figure 7. In this instance, the results are agnostic to the selected turbulence model, which provides a good shortcut.

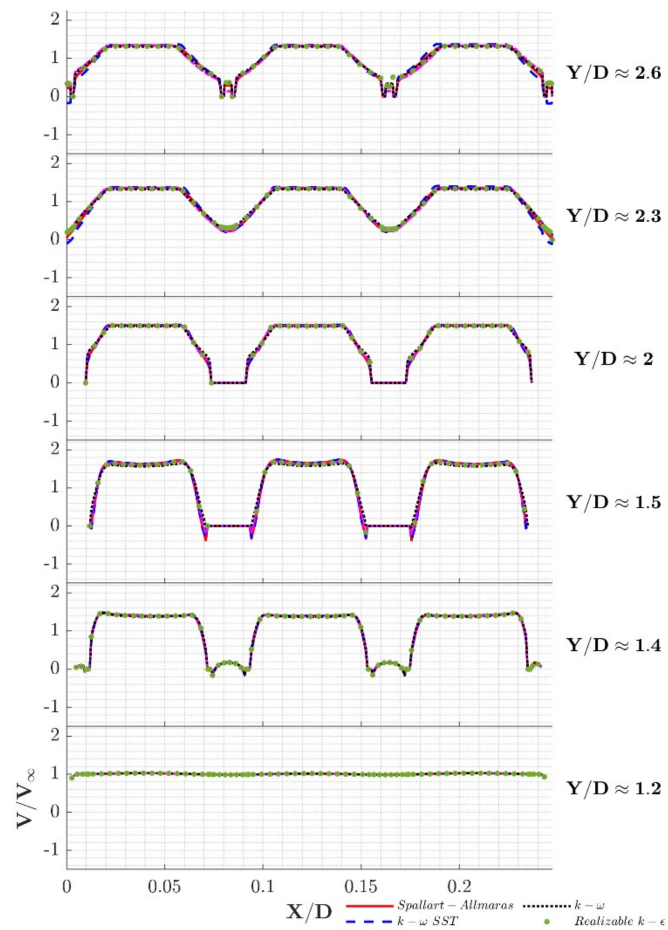

FIGURE 7: THE STREAMWISE EVOLUTION OF V/V_∞ WITH VARYING RANS MODELS.

However, even in system code models, it is also relevant to consider any potential bypass flow between the elements; this is where the U/V_∞ profiles become relevant. Consider the profiles shown in Figure 8, where initially, it seems that all the modules have nearly perfect agreement leading up to the legs at $Y/D \approx 1.4$, which ceases to be the case directly downstream of the legs where the flow separation occurs. Directly downstream of the separation at $Y/D \approx 1.5$, that the SST model predicts the largest spanwise velocities, which indicates more dramatic separation in comparison with the other models. This is particularly relevant when comparing the SST profile to the one predicted by the standard k-ω model. Interestingly enough, standard k-ϵ performs nearly identically to RKE (realizable k-ϵ) prior-to and throughout the flow separation until the flows exit the legs to mix, where k-ϵ shows a dramatically different profile to RKE and all other models as observed in the $Y/D \approx 2.3$ profiles.

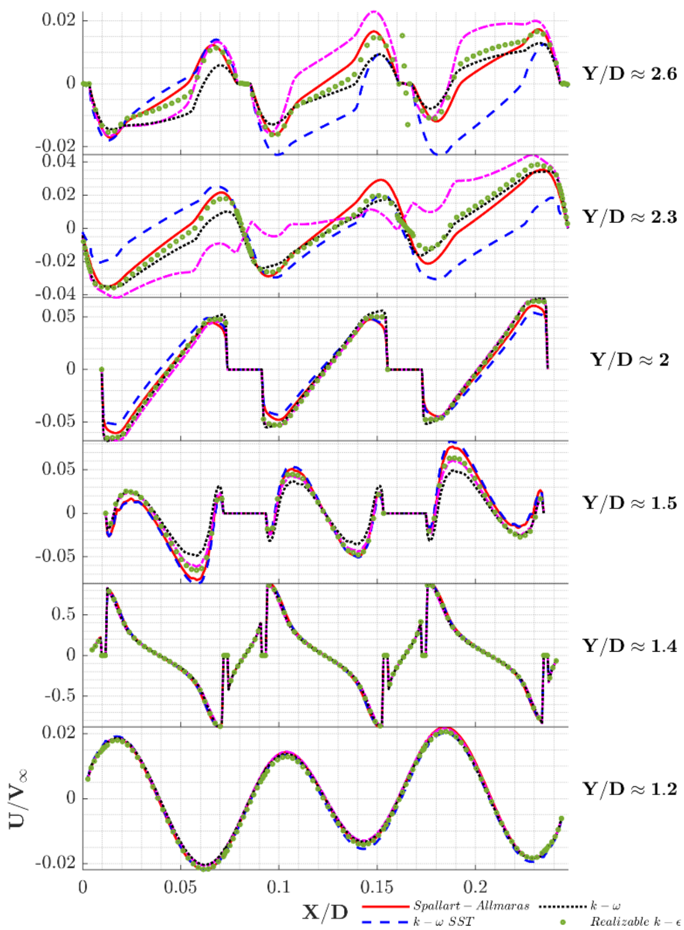

FIGURE 8: THE STREAMWISE EVOLUTION OF U/V_∞ WITH VARYING RANS MODELS.

The distinct deviation between the models, which can be observed in the intermediate mixing plenum trace ($Y/D \approx 2.3$) and directly upstream of the inlet to the fuel channels (top of the simulated geometry at $Y/D \approx 2.6$). The profiles at the top of the geometry have seemingly consistent counter-flow pairs of peaks for each assembly, where each pair has two peaks of similar magnitude and opposite directions (negative, positive). The left fuel assembly has approximate peaks at X/D~0.015 and 0.07, the middle assembly has the peak pairs of X/D~ 0.1 and 0.15, and the right assembly has the peak pairs of X/D~ 0.18 and 0.23. With the (approximate) peak pairs defined, it can be seen that k-ϵ predicts that the flow will be biased towards the right-most assemblies, while the SST models predicts that the flow will be biased towards the left-most assemblies. The other models predict nearly equal distributions, where the counter-flow peaks are nearly equal in magnitude. This observation is vital in interpreting the results from any of those models for inputting flow distributions into a system level code. This is particularly the case when considering the k-ϵ and the SST models results, where both of them show clear bias for one side of the core over the other. Note that the mesh and boundary conditions are identical in each of the models, which leaves only the turbulence formulae as the culprit for these deviations and biases.

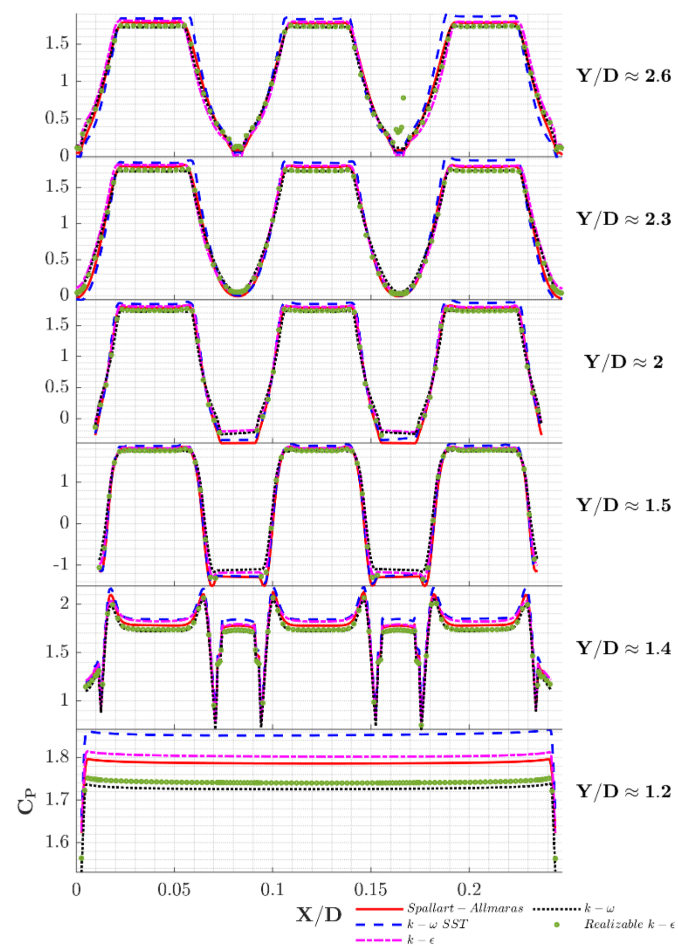

FIGURE 9: THE STREAMWISE EVOLUTION OF C_P WITH VARYING RANS MODELS.

Accurately assessing the pressure profiles is also of relevance when considering the flow distributions and the pressure drop across the core. Figure 9 assists in that domain, where the top-most profiles show practically model-agnostic results. A peculiarity can be observed with the RKE model at the interface between the middle and right assemblies (Figures 5 and 9), which is unique to the RKE model. It is unclear what caused this, but it may be a sign that additional mesh refinement is needed for that model. As opposed to the velocity profiles, the C_P profiles start out different, and then equalize as the flow progresses further downstream. This is intriguing because the mesh and inlet conditions are identical across all simulations, yet variations can be observed closer to the inlet. Considering that the pressure is very difficult to model accurately with RANS, it is likely that this is a RANS limitation in how each of the models uniquely handles pressure, but more studies would be necessary to confirm this suspicion.

4. CONCLUSION

CFD simulations were performed in for characterizing the inlet region of the NNS core. A mesh was iteratively refined until a converged solution for the streamwise velocity was reached, which was then used for modeling the flow using 5 different turbulence models that were explained in detail. The results show that the turbulence models provide nearly identical streamwise flow distributions throughout the geometry but differ considerably when analyzing the spanwise velocities. The spanwise velocities show significant variations in the velocity profiles, specifically in the intermediate mixing plenum. When observing the qualitative profiles, it was difficult to discern the variations between the predictions made by each model, but a statistical analysis shows that the minimum and maximum velocities can vary by upwards of 20 % in certain locations. The pressure is found to vary within approximately 5% between the models, which is the likely culprit in variations in the velocities.

A more detailed analysis of the predictions discrepancies is needed throughout the geometry, where comparing specific locations in the mixing plenum from one model to the next show upwards of 100 % variation in the velocities and pressures. This will be further investigated in future works. Considering the results in this analysis, the simulation predictions can vary considerably depending on the selected turbulence model, which provides a higher level of uncertainty when considering CFD results in this work. It is likely that a higher fidelity model, such as an LES model, may be needed to further verify the results. A validation is also necessary for both RANS and any higher fidelity model, which may require experimental testing efforts in the future.

ACKNOWLEDGEMENTS

The identification of certain commercial equipment, instruments, or materials does not imply recommendation or endorsement by the authors or by the National Institute of Standards and Technology. Contributions of NIST are not subject to copyright in the United States.

REFERENCES

[1] Şahin, D., et al., 2022, "NIST Neutron Source Preconceptual Design", In RERTR 2022 – 42nd International Meeting on Reduced Enrichment for Research and Test Reactors, October 3-5, 2022.

[2] Cook, J.C., et al., 2022, "Proposed NIST Neutron Source User Facility", Transactions of the American Nuclear Society, ANS Winter Meeting, November 13-17, 2022.

[3] Baroukh, I.R., Gurgen, A., Shen, J.S., Weiss, A.G., 2022, "A Preliminary Thermal-hydraulics Analysis for the NIST Neutron Source", Transactions of the American Nuclear Society, ANS Winter Meeting, November 13-17, 2022.

[4] Weiss, A.G., Gurgen, A., Baroukh, I.R., Shen, J., 2023, "Sensitivity Analyses of the Thermal-hydraulics Safety Margins in the Proposed NIST Neutron Source Design", In Proceedings of the 30th International Conference on Nuclear Engineering, Kyoto, Japan, May 21-26, 2023.

[5] Baroukh, I.R., Gurgen, A., Shen, J.S., Weiss, A.G., 2022, "Preliminary CFD Investigations for the NIST Neutron Source", Transactions of the American Nuclear Society, ANS Winter Meeting, November 13-17, 2022.

[6] ANSYS FLUENT, 14.5, 2014, "User's and theory guide", Canonsburg, Pennsylvania, USA: ANSYS, Inc.

[7] Weller, H.G., Tabor, G., Jasak, H., Fureby, C., 1998, "A Tensorial Approach to Computational Continuum Mechanics Using Object-Oriented Techniques", Computers in Physics 12(6): 620-631.

[8] Boussinesq, J., 1877, "Essai sur la théorie des eaux courantes", Mémoires présentés par divers savants à l'Académie des Sciences 23(1): 1-680.

[9] Schmitt, F.G., 2007, "About Boussinesq's turbulent viscosity hypothesis: historical remarks and a direct evaluation of its validity", Comptes Rendus Mécanique 335(9-10): 617-627.

[10] Launder, B.E., Sharma, B.I., 1974, "Application of the Energy Dissipation Model of Turbulence to the Calculation of Flow Near a Spinning Disc", Letters in Heat and Mass Transfer 1(2): 131-138.

[11] Wilcox, D.C., 1988, "Re-assessment of the scal-determining equation for advanced turbulence models", AIAA Journal 26(11): 1299-1310.

[12] Spalart, P.R., Allmaras, S.R., 1992, "A One-Equation Turbulence Model for Aerodynamic Flows", In 30th Aerospace Sciences Meeting and Exhibit, p. 439.

[13] Dacles-Mariani, J., Zilliac, G.G., Chow, J.S., Bradshaw, P., 1995, "Numerical/Experimental Study of a Wingtip Vortex in the Near Field", AIAA Journal 33(9): 1561-1568.

[14] Menter, F.R., 1994, "Two-Equation Eddy-Viscosity Turbulence Models for Engineering Applications", AIAA Journal 32(8): 1598-1605.

[15] Shih, T.H., Liou W.W., Shabbir, A., Yang, Z., Zhu, J., 1995, “A New k-ϵ Eddy Viscosity Model for High Reynolds Number Turbulent Flows”, Computers & Fluids 24(3): 227-238.

[16] Johnson, D.A., King, L.S., 1985, “A Mathematically Simple Turubulence Closure Model for Attached and Separated Turbulent Boundary Layers”, AIAA Journal 23(11): 1684-1692.

[17] Fradeneck, A.D., Kimber, M.L., 2020, “Applicability of Common RANS Models for the Calculation of Transient Forced to Natural Convection”, Journal of Verification, Validation and Uncertainty Quantification 5(2), p. 021003.

[18] Shih, T.H., Zhu, J., Lumley, J.L., 1994, “A New Reynolds Stress Algebraic Equation Model”, NASA Technical Memorandum 106644.

[19] Weber, D.P., et al., 2017, “High-Fidelity Light Water Reactor Analysis with the Numerical Nuclear Reactor”, Nuclear Science and Engineering 155(3): 395-405.

